



<http://www.diva-portal.org>

This is the published version of a paper published in .

Citation for the original published paper (version of record):

Enevold, J., Dahlberg, T., Stangner, T., Tang, S., Lindh, E M. et al. (2020)
Tunable two-dimensional patterning of a semiconducting C₆₀ fullerene film using a
spatial light modulator
ACS Applied Nano Materials, 3(6): 2574-0970
<https://doi.org/10.1021/acsanm.0c00793>

Access to the published version may require subscription.

N.B. When citing this work, cite the original published paper.

Permanent link to this version:

<http://urn.kb.se/resolve?urn=urn:nbn:se:umu:diva-166406>

Tunable Two-Dimensional Patterning of a Semiconducting and Nanometer-Thin C₆₀ Fullerene Film Using a Spatial Light Modulator

Jenny Enevold, Tobias Dahlberg, Tim Stangner, Shi Tang, E. Mattias Lindh, Eduardo Gracia-Espino, Magnus Andersson, and Ludvig Edman*



Cite This: *ACS Appl. Nano Mater.* 2020, 3, 5463–5472



Read Online

ACCESS |



Metrics & More



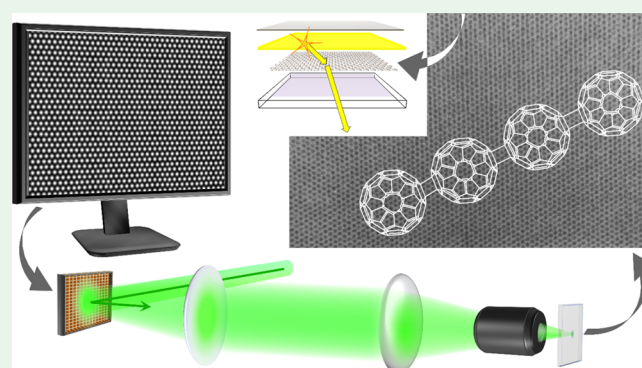
Article Recommendations



Supporting Information

ABSTRACT: The photochemical coupling of fullerene molecules into covalently connected oligomeric or polymeric structures can result in drastically lowered solubility in common solvents with retained semiconductor properties. Here, we exploit this combination of properties for the utilization of fullerenes as a negative photoresist material with electronic functionality. Specifically, we develop an easily tunable exposure system, essentially comprising a laser and a computer-controlled spatial light modulator (SLM) featuring >8 million independently controlled pixels, for the spatially selective photochemical transformation of nanometer-thin C₆₀ fullerene films. With a carefully designed laser-SLM-exposure/solvent-development cycle, we are able to realize well-resolved two-dimensional hexagonal or square patterns of circular C₆₀ microdots with a center-to-center distance of 1–5 μm and a maximum thickness of 20–35 nm over several square-millimeter-sized areas on a substrate. The functionality of such a hexagonal C₆₀ pattern was demonstrated by its inclusion in between the transparent electrode and the active material in a light-emitting electrochemical cell, which featured an enhanced light output by >50% in comparison to a reference device void of the patterned C₆₀ layer.

KEYWORDS: C₆₀ fullerenes, tunable and high-resolution 2D patterning, spatial light modulator, negative photoresist, light outcoupling, light-emitting electrochemical cell



INTRODUCTION

The field of organic electronics is in rapid development because of the easy tunability, soft and flexible nature, and facile processing of the constituent organic semiconductor (OSC).^{1–3} However, the ability to pattern a nanometer-thin OSC layer with retained electronic properties is an additional critical requirement for the function, or improved operation, of a number of applications, including photodetectors,^{4–6} sensors,^{7,8} emissive devices,^{9,10} and electronic circuits.^{11,12} It is therefore not surprising that a plethora of different patterning methods, such as transfer stamping,^{13,14} gravure printing,¹⁵ self-assembly,^{16–19} cross-linking by electron and ion beams,^{20,21} and photolithography using a sacrificial photoresist,^{22,23} have been developed during recent years.

The molecular nature of OSCs can further allow for a light-activated cross-linking of neighboring OSC molecules through the addition of a photoinitiator or by the endowment of the OSC with specific cross-linking units. If the photoactivation is executed in a spatially selective manner and the cross-linked OSC material features a different solubility than the nonexposed material, resist-free patterning of an OSC layer can be performed by a light-exposure/solvent-development

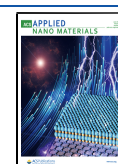
cycle. However, the unfortunate fact is that this approach commonly results in a notable lowering of the semiconductor functionality because of the existence of detrimental side-reaction residues and/or a disturbance of the conjugated system.^{24–28}

In this context, recent reports on that nonmodified and pristine fullerene semiconductors can be photochemically connected into dimeric,^{29–34} or polymeric,^{35–38} structures with an essentially retained electronic functionality are intriguing. Accordingly, with a spatially selective light exposure of a fullerene film through a shadow mask,^{32,33,39} or by two-beam laser interference,⁴⁰ followed by solution development, low-resolution two-dimensional (2D)^{32,33} or high-resolution one-dimensional⁴⁰ fullerene structures have been realized. These patterned fullerene films have demonstrated their

Received: March 23, 2020

Accepted: May 7, 2020

Published: May 7, 2020



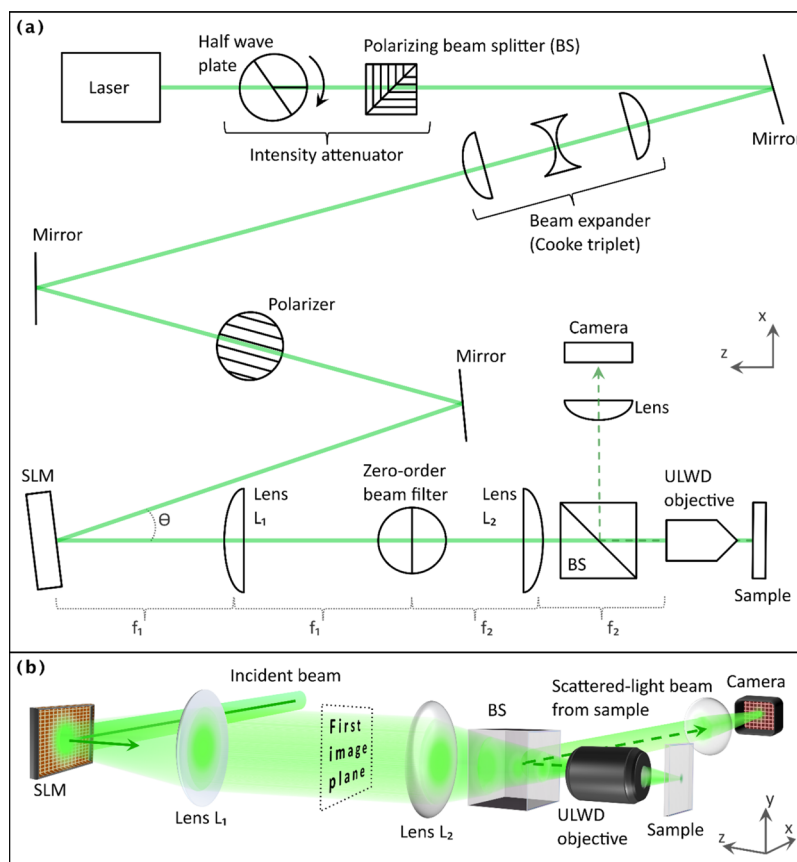


Figure 1. Top-view schematic (a) and a 3D schematic (b) presenting the exposure setup. f_1 and f_2 are the focal lengths of lenses L_1 and L_2 , respectively, and the zero-order beam filter is a stretched metal wire in a rotational mount, which is placed in the first image plane, that is, the common focal plane of the two lenses. Light beams rejected into beam dumps by the BS cubes and the zero-order beam filter in (b) are omitted for clarity.

semiconductor function as the active material in field-effect transistors,³³ inverters,³² and oscillators.⁴¹

Here, we report on the attainment of an easily modified and high-resolution 2D fullerene pattern with well-defined micron- and nanosized features over a large area, using an exposure system essentially comprising a laser and a computer-controlled spatial light modulator (SLM) and subsequent solvent development. We specifically realize large-area 2D hexagonal and square patterns of C_{60} fullerene microdots with a maximum thickness of 20–35 nm and with a center-to-center distance of 1–5 μm , which were subsequently utilized for the attainment of a significantly improved outcoupling from a surface-emitting light-emitting electrochemical cell (LEC). We emphasize that the attained semiconducting fullerene pattern features a high resolution, is well replicated over a large area, and is easily modified by the computer input.

EXPERIMENTAL SECTION

The C_{60} powder (>99.5%, Solenne) was used as received. A 40 nm-thick C_{60} film was thermally evaporated at a base pressure of $<5 \times 10^{-6}$ mbar (Univex 350 G, Leybold) onto carefully cleaned glass substrates (Thin Film Devices). The 40 nm thickness was confirmed with contact profilometry (DektakXT Bruker) on a mechanically scratched C_{60} film. The C_{60} -coated substrate was mounted in a custom-made holder under N_2 in a glovebox ($[O_2]$, $[H_2O] < 1$ ppm), and the holder was sealed air-tight with a 0.2 mm-thick antireflection-coated glass window (diameter = 30 mm, VIS 0° coated, Ultra-Thin N-BK7 Window 66-189, Edmund Optics).

The C_{60} film in the sample holder was transferred to the exposure setup described in Figure 1. The light source was a linearly polarized, continuous-wave green laser ($\lambda = 532$ nm, peak output = 1500 mW, Cobolt Samba), and the intensity attenuator comprised a zero-order half-wave plate ($\lambda = 532$ nm, WPH05M-532, Thorlabs) and a high-power polarizing beam splitter (BS) cube ($\lambda = 532$ nm, PBS12-532-HP, Thorlabs). In order to expand the beam diameter to fit the active area of the SLM (90% of the total chip size, limited by the shorter axis being 9.22 mm, resulting in a beam diameter of 8.3 mm), a Cooke triplet beam expander was used. It comprised a biconcave lens ($f = 15.0$ mm, AR-coated for $\lambda = 350$ –700 nm, LD2060-A, Thorlabs) inserted between two plano-convex lenses ($f = 60$ mm, LA1134-A, and 250 mm, LA1461-A, both AR-coated for $\lambda = 350$ –700 nm, Thorlabs). The polarizer was a linear polarizer with N-BK7 windows ($\lambda = 400$ –700 nm, LPVISE100-A, Thorlabs), and the computer-controlled phase-only SLM (GAEA-2, Holoeve) featured 3840×2160 independently controlled active pixels. The two lenses L_1 and L_2 (AR-coated for $\lambda = 350$ –700 nm, Thorlabs) in the 4f configuration, featuring focal lengths of 250 mm (LA1301-A) and 100 mm (LA1050-A), were chosen to reduce the beam size from 8.3 mm at the SLM to fit the back aperture diameter of the objective of 3.38 mm (as calculated from $2 \times f_{\text{OBJ}} \times \text{NA}_{\text{OBJ}}$). The zero-beam filter was a tightly stretched copper thread ($d = 0.25$ mm), the ultralong working distance (ULWD) objective featured 80 \times magnification ($f = 180$, MS-plan 80 \times /0.75, IC 80, Olympus), and the camera was a 3.0 USB color camera (1/3", 1328 \times 1048 pixels, Flea3, Point Grey Research). The effective exposure intensity incident on the C_{60} film was measured with a power meter (model PM100D equipped with an S401C sensor, Thorlabs) at the position of the film surface.

The exposure pattern was designed with the freeware image editor Gimp in the form of a 1600 \times 1600 pixel png raster graphics image. A

Fourier transformation of the exposure pattern into a 3840×2160 pixel phase mask was executed with Holoeye SLM Pattern Generator software. This phase mask controls the positions of the corresponding 3840×2160 pixels of the SLM. In order to minimize noise, we prepared 100 different phase-mask images (that essentially produced the same exposure pattern) that were input sequentially to the SLM at a 10 Hz repetition rate.

The development of the exposed C_{60} film was performed by opening the sample holder in the ambient and immersing the exposed C_{60} film in toluene (anhydrous 99.8%, Sigma-Aldrich) for ~ 10 s. After the solvent immersion step, the C_{60} film was flushed with 2-propanol and blown dry with pressurized air. The height of the C_{60} microdot features was determined by the selected values for the modulated laser beam intensity and the exposure time during the exposure step (and the thickness of the deposited film). We found that a modulated laser beam intensity of 10 W/cm^2 and an exposure time of 10 s resulted in a C_{60} microdot height of ~ 30 nm.

The optical micrographs were recorded with an optical microscope operating in the phase-contrast mode (Zeiss Axio Imager Z1 microscope, TL Phase channel in the software ZEN), using two different objectives ($10\times/0.30$ Ph1 and $40\times/0.75$ Ph2 EC-plan-Neofluar objectives). The atomic force microscopy (AFM) images were captured with a Bruker BioScope Catalyst microscope operating in the tapping mode (PeakForce QNM) using a soft material tip (FESP, Veeco).

LEC fabrication and characterization were performed in N_2 -filled gloveboxes ($[O_2]$, $[H_2O] < 1$ ppm). The active-material ink comprised an electroluminescent conjugated copolymer termed Super Yellow (Merck catalogue number PDY-132), a hydroxyl-terminated trimethylolpropane ethoxylate (TMPE-OH, Aldrich, $M_w = 450$ g/mol) for the ion-transport material, and the salt KCF_3SO_3 (Aldrich) dissolved in anhydrous cyclohexanone in a mass ratio of Super Yellow/TMPE-OH/ $KCF_3SO_3 = 1:0.15:0.03$. The active-material ink was either spin-coated on top of a patterned C_{60} layer on an indium tin oxide (ITO)-coated glass substrate ($20 \Omega \text{ sq}^{-1}$, Thin Film Devices) or directly spin-coated on top of the ITO-coated glass substrates for the reference LEC. The thickness of the dry active material was 170 nm.

The first stitching unit for the thin patterned C_{60} layer was exposed to a laser intensity of 9.5 W/cm^2 for 9 s, while the first unit for the thick patterned C_{60} layer was exposed to a laser intensity of 10 W/cm^2 for 12 s. It proved critically important to remove all soluble C_{60} residues from the patterned C_{60} layer before spin coating of the active material, and this was effectuated by a twice repeated cycle of 10 s immersion in toluene followed by 10 s immersion in cyclohexanone ($\geq 99.5\%$, Sigma-Aldrich) before the spin coating. A 100 nm-thick Ag top electrode was deposited on top of the active material by thermal vacuum evaporation at a base pressure of $< 5 \times 10^{-6}$ mbar (Univex 350 G, Leybold). More details on the fabrication of the reference LEC can be found in ref 42.

The LEC devices were driven and electrically characterized with a computer-controlled source-measure unit (Agilent U2722A). The luminance was measured with a calibrated photodiode, equipped with an eye-response filter (S9219-01, Hamamatsu Photonics), and connected to an embedded evaluation board (myRIO-1900, National Instruments) via a current-to-voltage amplifier. The angle-dependent electroluminescence (EL) spectrum was measured with a custom-built goniospectrometer, comprising a fiber-optic charge-coupled device-array spectrometer (Flame-S, Ocean Optics) and a stepper motor, controlled by a LabVIEW virtual instrument.^{43,44} The edges of the LEC devices were blackened with a permanent marker pen to eliminate detection of wave-guided modes. The LEC devices were driven by a constant current density of 50 mA/cm^2 for the luminance measurements and by 30.8 mA/cm^2 for the spectral measurements.

The optical simulation of the LEC devices was performed with the software Setfos 4.6.11 from Fluxim (<http://www.fluxim.com>), which is based upon the transfer matrix formalism. The simulated device configuration comprises the following stack of planar layers (with the thickness specified in parenthesis): glass substrate (0.7 mm), ITO (145 nm), C_{60} (15/25 nm), active material (170 nm), and Ag (100

nm). The steady-state doping structure in the active material was simulated by constant p-type and n-type doping gradients (with the largest p- and n-type doping concentrations at the anode and cathode, respectively), separated by a 30 nm-wide intrinsic region, using the procedure outlined in ref 43. The excitons were positioned in the center of the emission zone and featured an isotropic dipole orientation. In order to determine the position of the intrinsic region in the interelectrode gap, we simulated the EL spectra as a function of viewing angle for a number of different values for the intrinsic region position and calculated the root-mean-square deviation (rmsd) between the simulated and measured spectra. The selected value for the position of the intrinsic region corresponded to the lowest rmsd value (see Figure S4b,d). For the wavelength-dependent values for the refractive index and the extinction coefficients, we either used values provided by Setfos or values from the literature (C_{60} ⁴⁵ and Super Yellow as a function of doping⁴³).

RESULTS AND DISCUSSION

Figure 1 is a schematic presentation of the exposure setup. The light source is a continuous-wave green laser that emits linearly polarized light with a wavelength of $\lambda = 532$ nm. The intensity of the laser light is modulated using an intensity attenuator, which comprises a rotatable half-wave plate and a polarizing BS; the orientation of the former determines the ratio between the vertically and horizontally polarized components of the laser beam, while the latter selectively reflects away the vertical component. One advantage with this setup is that it is possible to drive the laser at its most stable maximum output power and downregulate to the desired intensity (typically 70% of the maximum output) with the intensity attenuator. A Cooke triplet beam expander⁴⁶ is employed for enlarging the horizontally polarized laser beam so that it matches the area of the SLM display ($15.32 \times 9.22 \text{ mm}^2$). The SLM comprises 3840×2160 pixels, which are independently controlled by a computer. The angle θ between the incident and the reflected laser beams on the SLM is designed to be low (here $\sim 7^\circ$) to minimize the fraction of light entering the SLM in one pixel and exiting in another.

Figure 1a shows that the lenses L_1 and L_2 with focal lengths f_1 and f_2 , respectively, are organized in the so-called 4f design,⁴⁷ which implies that the “first image plane” of the SLM-generated laser pattern (see Figure 1b) appears at the common focal plane of the two lenses. This further requires that the SLM be positioned at a distance of f_1 from L_1 . The undesired zero-order beam can then be removed by the inclusion of a zero-order beam filter at the position of the first image plane. A further suppression of the undesired zero-order beam is obtained by tuning the dichroic-film polarizer positioned before the SLM in the beam path. The polarizer is placed after the beam expander in order to not exceed its damage threshold.

A ULWD objective is positioned at a distance f_2 from L_2 so that the designed exposure image is appropriately focused onto the surface of the fullerene film to be patterned (the sample); the latter is mounted in a N_2 -filled gas-tight sample holder and optically accessed for exposure through an antireflection-coated cover glass. In order to minimize aberrations in the projected exposure image on the surface of the fullerene film, the cover glass should be as thin as possible (here 0.2 mm). The exact positioning of the fullerene film in the sample holder with respect to the ULWD objective is controlled by an x - y - z stage with tilt adjustment.

A fraction of the exposure light is scattered off the fullerene film, returned back through the objective, and directed to a

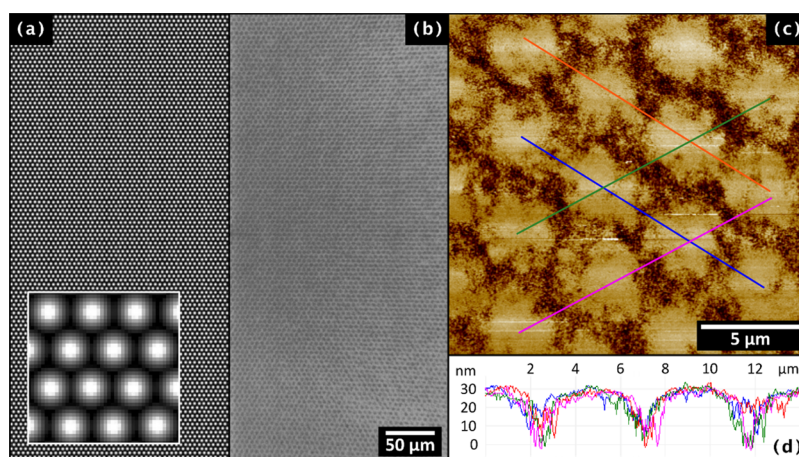


Figure 2. (a) Computer-generated hexagonal circular-dot pattern, with the white regions corresponding to the areas to be exposed to the laser-SLM output. The inset shows a close-up of the exposure pattern. (b) Optical microscopy image of a portion of the patterned $240 \times 480 \mu\text{m}^2$ array of C_{60} microdots on a glass substrate. (c) AFM image presenting a close-up of the patterned C_{60} microdot array. (d) Four overlapping height profiles of neighboring C_{60} microdots, as derived from the four traces marked with the correspondingly colored lines in (c).

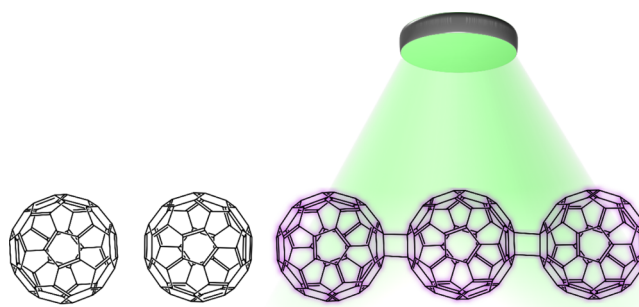
probing camera by a BS cube and a lens. The camera image then allows for an appropriate inspection of the exposure image on the fullerene film at very low laser intensity ($\sim 1 \text{ mW/cm}^2$) so that the focus of the exposure system can be adjusted without inducing undesired premature photochemical reactions within the fullerene film. Specifically, the exact positioning of the optical elements in the exposure beam path for a well-focused exposure was performed in two steps: (i) by the observation of an externally illuminated dust particle on a flat surface at the location of the fullerene film and (ii) by the observation of an SLM-generated laser exposure pattern on the same surface. The camera image also enabled for improved alignment of the polarizer positioned before the SLM so that the zero-order beam is minimized.

Figure 2a presents the digital light-exposure pattern (prepared in a raster graphics editor) to be delivered by the laser-SLM setup. The close-up in the inset shows that the selected exposure pattern comprises circular dots organized in a hexagonal pattern. The exposure pattern is then Fourier-transformed into a 3840×2160 pixelated “phase mask” image (using the SLM pattern generator software), which controls the positions of the corresponding 3840×2160 pixels in the SLM. In order to minimize noise, we prepared 100 different phase-mask images (that essentially produced the same exposure pattern) that were input sequentially to the SLM at a 10 Hz repetition rate.

A C_{60} fullerene film with 40 nm thickness was deposited on a glass substrate by thermal vacuum evaporation. The C_{60} film on the glass substrate was mounted into the N_2 -filled sample holder for the laser-SLM exposure, which was performed at a typical exposure intensity of $\sim 10 \text{ W/cm}^2$ and lasted between 5 and 20 s in different experiments. The exposed C_{60} molecules are (primarily) transformed into linear polymers, as depicted in Scheme 1. The exposed C_{60} film was thereafter developed by immersion into a toluene development solution for $\sim 10 \text{ s}$, which selectively removed the nonexposed parts of the film (i.e., the regions that comprised nonexposed C_{60} monomers).

We mention that it is possible to perform this exposure/development patterning also with other fullerenes, such as [6,6]-phenyl- C_{61} -butyric acid methyl ester (PCBM). However, an important advantage with C_{60} is that it can form long-chain polymers during the light exposure (whereas, e.g., PCBM

Scheme 1. The Exposure Step that Constitutes a Spatially Selective Photochemical Transformation of the C_{60} Molecules in the Film^a



^aSpecifically, the laser light is modulated by the SLM setup so that it selectively exposes some of the C_{60} monomers (the three to the right in the schematic), which are photochemically transformed into (primarily) linear polymers. The subsequent development step (not shown) will selectively remove the nonexposed fullerene monomers (the two to the left in the schematic) by dissolution into the development solution.

solely forms dimers) and that the solubility contrast between the C_{60} polymers and monomers accordingly is very high in many solvents.

Figure 2b presents an optical microscopy image of a representative portion of a patterned C_{60} film on a glass substrate. It is notable that the 2D hexagonal microdot pattern is well replicated over the entire film area. Figure 2c shows a close-up of the microdot pattern recorded with AFM. The corresponding AFM line graphs depicted in Figure 2d reveal that the surface features are well repeated but somewhat rough on the nanometer scale. The AFM image also shows that the center-to-center distance and the height of the C_{60} microdots are $\sim 5 \mu\text{m}$ and $\sim 30 \text{ nm}$, respectively, in this experiment. The latter demonstrates that a significant fraction ($\sim 25\%$) of the C_{60} molecules was dissolved/removed by the development solvent also in the most heavily exposed region. In this context, we mention that evidence for the fact that the glass substrate is bare and free from C_{60} in the “valley” regions between the microdots was provided by AFM and profilometer thickness measurements on patterned fullerene films that were scratched

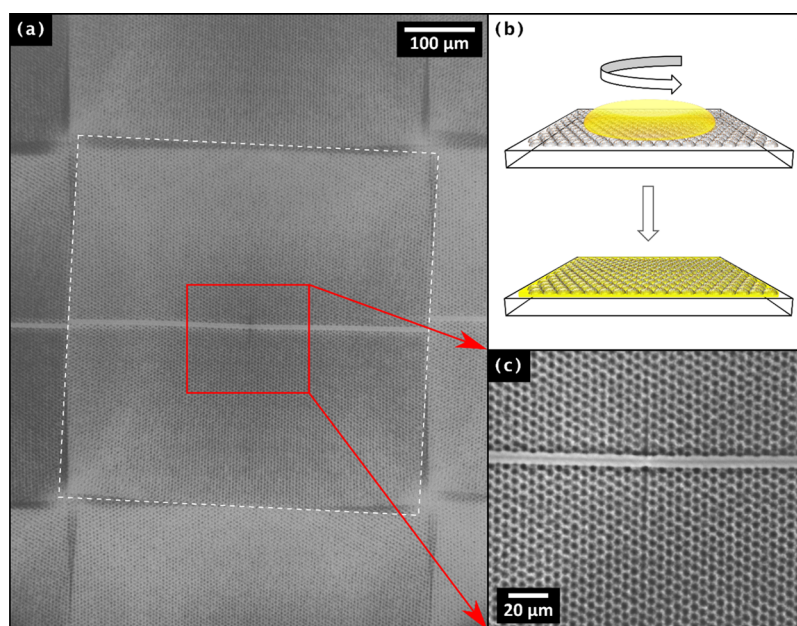


Figure 3. (a) Optical microscopy image of a select part of a large-area-patterned C_{60} film, comprising 12 separately patterned and stitched smaller areas. The white dashed square marks the center area. The horizontal line void of dot features in the center of each patterned area originates from the zero-order beam filter. (b) Schematic illustration of the spin coating of an electroluminescent active material on top of the patterned C_{60} layer. (c) High-magnification optical micrograph (recorded in the phase-contrast mode) of the spin-coated active material on top of the patterned C_{60} layer. The observed hexagonal pattern originates from the patterned C_{60} layer beneath and demonstrates that the active material is deposited in a nondestructive manner.

using a sharp stylus. (Note also that we and others⁴⁸ have shown that the density of the C_{60} film is left effectively invariant by the exposure step.) We find that the height of the patterned C_{60} microdots can be determined by the exposure intensity (as effectively controlled using the intensity attenuator in Figure 1a) and/or the exposure time. We have also fabricated other patterns with a higher resolution, and a scanning electron microscopy image of a square C_{60} microdot pattern with a center-to-center distance of $\sim 1.5 \mu\text{m}$ is displayed in Figure S1.

The largest fullerene film area that can be exposed by our laser-SLM setup is limited by the ULWD objective (see Figure 1) and constitutes a circle with a diameter of $700 \mu\text{m}$. For the attainment of a larger uniformly patterned area, we instructed the SLM software to produce a square-shaped exposure-pattern region, with an edge length of $490 \mu\text{m}$ (corresponding to 113×100 C_{60} microdots), which was positioned in the center of this circle. The circular “frame” region encompassing the square was set to be “black”, that is, it left the film nonexposed. Several such exposed square regions were stitched together into a larger uniformly exposed area by moving the C_{60} sample holder stage in the x - and y -directions with a step length of $490 \mu\text{m}$. Figure 3a is an optical micrograph of a select portion of the correspondingly $1960 \mu\text{m} \times 1470 \mu\text{m}$ patterned C_{60} film fabricated by this stitching procedure.

The thin horizontal lines void of the patterned material in the center of each pattern unit originate from the zero-order beam filter. These zero-order reflections from the SLM can be eliminated with elaborate engineering approaches,^{49,50} but such refinement procedures were outside the scope of this study. The observed minor overlap between different pattern areas is due to a slight tilt of the sample in the x - y direction between the different exposures.

The temperature of the C_{60} film and the substrate was found to increase during the light exposure, which resulted in decreased photopolymerization efficiency.^{29,51} We compensated for this temperature-induced lowering of the polymerization efficiency in the stitching experiments by a gradual increase in the modulated laser beam intensity and by an extension of the exposure time. During the essentially uninterrupted sequential exposure of the 12 stitching units, shown in Figure 3a, the exposure intensity and the exposure time were gradually and synchronously increased to twice the initial values (10 – 20 W/cm^2 ; 10 – 20 s) in order to attain a uniform C_{60} pattern over the entire film area. An alternative could be to incorporate a temperature control system into the setup.

The functionality of the patterned C_{60} film was tested in an LEC. It was fabricated by first patterning the C_{60} film on an ITO-coated glass substrate, thereafter spin coating a high-performance active material⁴² on top of the patterned C_{60} (see Figure 3b), and finally depositing a Ag top electrode on top of the active material. The selection of Ag and ITO for the two electrodes was motivated by the fact that this electrode/active material combination is reported⁵² to allow for a relatively stable and efficient operation in both forward bias (with ITO as the positive anode) and in reverse bias (with ITO as the negative cathode).

A critical question relates to whether the C_{60} pattern survives the spin coating of the active-material ink, which comprises a blend of an electroluminescent conjugated polymer termed Super Yellow, a TMPE-OH ion transporting compound, and a KCF_3SO_3 salt dissolved in cyclohexanone. Figure 3c shows an optical micrograph recorded in the phase-contrast mode on the active-material-coated C_{60} pattern. The micrograph clearly reveals that the dry active material, as desired, coats the C_{60} pattern in a nondestructive and relatively conformal manner.

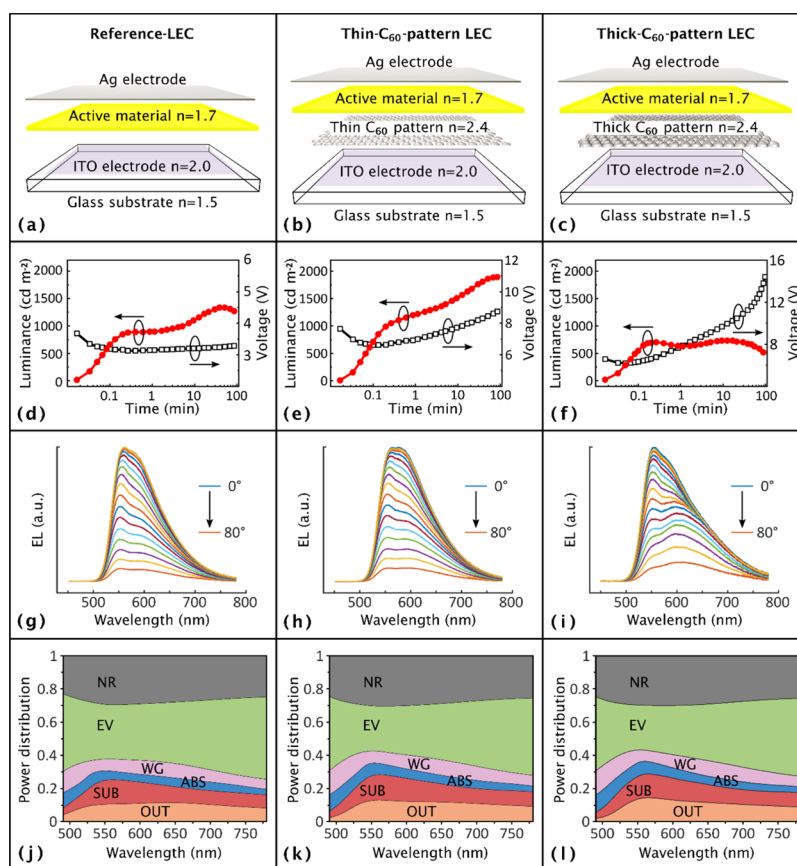


Figure 4. Device architecture for (a) the reference LEC void of the patterned C₆₀ layer, (b) the thin-C₆₀-pattern LEC with a 20 nm-thin patterned C₆₀ layer, (c) the thick-C₆₀-pattern LEC with a 35 nm-thick patterned C₆₀ layer. The below data are recorded on the device architecture identified at the top of the column. (d–f) Transient evolution of the luminance (red solid circles, left y-axis) and the drive voltage (black open squares, right y-axis). (g–i) EL spectrum at different viewing angles, as identified in the inset. (j–l) Simulated relative power contribution as a function of wavelength. The devices were driven in forward bias (i.e., with ITO as the positive anode) by a constant current density of 50 mA/cm².

We have also fabricated reference LECs, void of the patterned C₆₀ layer, in an identical manner. In line with the above-mentioned observation, we find that the C₆₀/active-material bilayer in the C₆₀-pattern LECs exhibits a larger average thickness than the single active material (with a thickness of 170 nm) in the reference LEC.

We also mention that we have fabricated and characterized a control device comprising a uniform (i.e., nonpatterned) C₆₀ layer in between the transparent ITO electrode and the active material but that the current was low and the light emission was absent in forward bias (with ITO as the positive anode). We rationalize this observation with the poor hole transport capacity of fullerenes.^{53–56} We finally mention that the attainment of a good LEC performance was found to be critically dependent on the complete removal of soluble (nonpolymerized) C₆₀ residues from the patterned C₆₀ layer before the spin coating of the active material. Otherwise, excitons formed on Super Yellow will be effectively split and quenched by an electron transfer to the low lowest unoccupied molecular orbital level of C₆₀^{57–59} molecules dispersed within the active material.

Figure 4a–c presents an exploded-view schematic of the three investigated device architectures: the “reference LEC” void of the patterned C₆₀ layer (a), a “thin-C₆₀-pattern LEC” with a 20 nm-thin patterned C₆₀ layer positioned between the transparent ITO electrode and the active material (b), and a “thick-C₆₀-pattern LEC” with a 35 nm-thick patterned C₆₀

layer sandwiched between the ITO and the active material (c). Corresponding device data are presented in the column below the device architecture. We have tested three independent devices for each of the two C₆₀-pattern LEC and two devices for the reference LEC, and the presented data are for the best performing device. We emphasize however that the device-to-device variation was minor and that the presented trends were invariant for all of the investigated devices.

Figure 4d–f displays the luminance and drive-voltage transients during forward bias driving with a constant current density of ~50 mA/cm². Note that the same current was applied in all experiments but that a slight variation of 5% of the emission area resulted in a corresponding slight variation for the current density. The extended long-term forward-bias operation of the reference LEC and the thin-C₆₀-pattern LEC is presented in Figure S2.

All forward-bias devices, as well as all reverse-bias devices (see Figure S3), exhibit an increase in luminance and a decrease in voltage during the initial operation. This temporal change is due to the initial electric double-layer formation and the subsequent electrochemical doping of the active material that is characteristic of a functional LEC device.⁶⁰ After the initial turn-on phase, the active material comprises a p–n junction, at which the injected electrons and holes recombine into excitons with high probability. These excitons can decay under the emission of photons.

It is thus established that all three devices feature the desired in situ formation of a p–n junction, but it is also clear that their performance is strongly dependent on the existence and thickness of the patterned C₆₀ layer. In forward bias, the thin-C₆₀-pattern LEC features the highest peak luminance (current efficacy) of 1910 cd/m² (4.0 cd/A), the reference LEC peaks at 1330 cd/m² (2.6 cd/A), and the thick-C₆₀-pattern LEC emits with the weakest maximum luminance of 740 cd/m² (1.4 cd/A). We also find that the thin-C₆₀-pattern LEC features the best long-term stability (see Figure S2). The trend for the minimum voltage is different because the reference LEC exhibits the lowest voltage of 3.1 V, while the thin-C₆₀-pattern LEC and thick-C₆₀-pattern LEC operate at higher voltages of 6.6 and 6.1 V, respectively. We attribute the higher drive voltage of the C₆₀-pattern LECs in forward bias to the fact that the C₆₀-covered regions at the ITO anode are inhibiting the hole injection because of the general poor hole transport capacity of fullerenes.^{53–56} In contrast, Figure S3 shows that the C₆₀-pattern LECs in reverse bias feature essentially the same drive voltage as the reference LEC, which importantly confirms that the semiconducting properties of C₆₀ are retained following the patterning procedure. However, the reverse-bias C₆₀-pattern LECs feature a markedly lower peak luminance, and our focus is therefore, from hereon, on the forward-bias devices.

In order to understand the high luminance of the forward-bias thin-C₆₀-pattern LEC, we have performed an extended device and optical-simulation study. Figure 4g–i presents the angle-dependent EL spectrum, captured after 15 min of operation. The reference LEC exhibits essentially the same EL spectrum for all viewing angles. The thin-C₆₀-pattern LEC features a similar invariant angular dependence, although the second vibronic peak at ~610 nm is slightly enhanced at small viewing angles. The situation is however distinctly different for the thick-C₆₀-pattern LEC, which features a strong relative enhancement of the second vibronic peak at large viewing angles and a corresponding relative depression of the same peak at small viewing angles. This observation implies that optical cavity effects start to play a significant role when the distance between the Al and ITO electrodes is increased by the inclusion of the patterned C₆₀ layer.

Further information on the steady-state behavior of the LEC devices was gleaned from optical modeling using the procedure outlined in refs 43 and 44 as a basis; see Experimental Section and Figure S4 for details. The employed commercial software Setfos (version 4.6.11) is designed to model 1D structures, comprising infinitely extended layers in the planar direction, and the C₆₀ pattern in the C₆₀-pattern LECs therefore had to be replaced by a uniform C₆₀ layer with constant thickness. The effective thickness for this uniform C₆₀ layer was 15 nm for the thin-C₆₀-pattern LEC and 25 nm for the thick-C₆₀-pattern LEC, as derived from the AFM data (see, e.g., Figure 2d). The location of the center of the emission zone (the p–n junction) was determined by fitting the simulated EL spectra to the experimental data in Figure 4g–i. Figure S4 shows that the center of the p–n junction is located closer to the Ag cathode for all devices. For the reference LEC, the center of the p–n junction is positioned 56 nm from the Ag cathode (and 114 nm away from the ITO anode). The inclusion of the C₆₀ layer results in a shift of the center p–n junction from the Ag cathode by 12 nm for both the thin-C₆₀-pattern LEC and thick-C₆₀-pattern LEC devices. The corresponding shift away

from the ITO anode is 3 nm for the thin-C₆₀-pattern LEC and 13 nm for the thick-C₆₀-pattern LEC.

Figure 4j–l presents the simulated steady-state power distribution as a function of wavelength, while Tables S1 and S2 summarize the forward and angular-integrated emission, respectively. The different optical modes are defined as follows: “OUT” denotes the outcoupled modes that are visible to an external observer, “SUB” denotes the glass substrate modes, “ABS” is the light lost to linear absorption, “WG” denotes the wave-guided modes traveling in the active material and the ITO, “EV” denotes the evanescent modes (i.e., losses due to near-field absorption and coupling of excitons to nonemissive surface plasmons at the electrode interfaces), and “NR” denotes the nonradiative modes.

The most significant result of the simulation is that the fraction of “useful” outcoupled light is predicted to increase by ~15–30% following the inclusion of a C₆₀ layer. More specifically, the simulation shows that the losses to linear absorption, as expected, are increasing with an absorbing C₆₀ layer included in the photon path⁶¹ but that this increased loss is more than compensated by the marked lowering of the evanescent modes. We assign the suppression of the evanescent losses to the increased separation of the excitons (formed in the p–n junction region) from the electrodes, primarily the top Ag electrode, following the inclusion of the C₆₀ layer.

We note that the simulation underestimates the experimentally observed luminance increase following the inclusion of the thin C₆₀ pattern layer and therefore suggests that the nonflat interface between the optically distinct^{61–67} C₆₀ and active-material layers (see Figures 4a–c and S5) results in randomization of the directions of the photon paths,^{68–73} which increases outcoupling at the ITO/glass and glass/air interfaces. The experimental data in Figure 4d–f further show that the thick-C₆₀-pattern LEC features a lower luminance than the reference LEC, which we tentatively attribute to the local high current density, with a concomitant increase in polaron and exciton quenching reactions, at the narrow C₆₀-free regions at the ITO/active-material interface.

These results thus imply that the selected thickness of the patterned C₆₀ layer results in a delicate balance between increased light emission because of suppression of evanescent modes and randomization of the light cone and lowered emission efficiency because of a confined transport region. Nevertheless, it is clear that the inclusion of an appropriately designed patterned C₆₀ layer can result in a significant boost of the light emission from an LEC device comprising a single-layer active material and two air stable electrodes.

CONCLUSIONS

To summarize, we present a straightforward and easily tunable method for the fabrication of high-resolution, 2D semiconducting fullerene patterns over large areas. The spatially selective photochemical transformation of the fullerene film (the exposure) is performed with an optical system essentially comprising a laser and an SLM, while the subsequent development is effectuated by immersion into a development solution. We anticipate that the entire exposure/development cycle can be executed within a time frame of 10 s in a scaled-up and automated setup. It is notable that the presented patterning method does not employ sacrificial photoresist materials, cumbersome shadow masks, or expensive printing stamps and cylinders and that the photochemical trans-

formation of the fullerene semiconductor is executed without a preceding chemical functionalization or by the addition of performance-degrading additives. It is further notable that pattern selection is effectuated by the computer input to the SLM and that a large number of different patterns therefore are easily accessible. We finally exemplify the functionality of a fabricated square-millimeter-sized patterned C₆₀ fullerene film, featuring a hexagonal array of microdots with a center-to-center distance of 5 μm and a peak thickness of 20 nm, by its inclusion into a LEC device. Such a device equipped with the C₆₀ microdot layer in between the transparent electrode and the active material features a 50% increase in light emission output compared to a reference device void of the patterned C₆₀ layer.

■ ASSOCIATED CONTENT

Supporting Information

The Supporting Information is available free of charge at <https://pubs.acs.org/doi/10.1021/acsanm.0c00793>.

SEM image of the patterned C₆₀ microdot array, with microdots positioned in a square lattice with the shortest center-to-center distance of $\sim 1\ \mu\text{m}$; device performance of the reference LEC and thin-C₆₀-pattern LEC during reverse-bias operation; comparison of measured and simulated EL spectra for determination of the emission zone position; simulated enhancement by inclusion of the patterned C₆₀ layer in LEC devices; simulated power distribution in the reference LEC and C₆₀-pattern LECs; and refractive index as a function of wavelength for the active-material constituents (PDF)

■ AUTHOR INFORMATION

Corresponding Author

Ludvig Edman – The Organic Photonics and Electronics Group, Department of Physics, Umeå University, SE-90187 Umeå, Sweden; orcid.org/0000-0003-2495-7037; Email: ludvig.edman@umu.se

Authors

Jenny Enevold – The Organic Photonics and Electronics Group, Department of Physics, Umeå University, SE-90187 Umeå, Sweden

Tobias Dahlberg – The Biophysics and Biophotonics Group, Department of Physics, Umeå University, SE-90187 Umeå, Sweden

Tim Stangner – The Biophysics and Biophotonics Group, Department of Physics, Umeå University, SE-90187 Umeå, Sweden

Shi Tang – The Organic Photonics and Electronics Group, Department of Physics, Umeå University, SE-90187 Umeå, Sweden

E. Mattias Lindh – The Organic Photonics and Electronics Group, Department of Physics, Umeå University, SE-90187 Umeå, Sweden; orcid.org/0000-0002-1903-9875

Eduardo Gracia-Espino – The Organic Photonics and Electronics Group, Department of Physics, Umeå University, SE-90187 Umeå, Sweden; orcid.org/0000-0001-9239-0541

Magnus Andersson – The Biophysics and Biophotonics Group, Department of Physics, Umeå University, SE-90187 Umeå, Sweden; orcid.org/0000-0002-9835-3263

Complete contact information is available at: <https://pubs.acs.org/doi/10.1021/acsanm.0c00793>

Notes

The authors declare no competing financial interest.

■ ACKNOWLEDGMENTS

We gratefully acknowledge Dr. Sandra Jenatsch at Fluxim for valuable input with regard to the simulations, Petter Lundberg and Sandra Mattsson at Umeå University for appreciated assistance with measurements, and Prof. Reinhard Carius and Dr. Johan Zakrisson for helpful discussions regarding the exposure setup. The Biochemical Imaging Center at Umeå University and the National Microscopy Infrastructure, NMI (VR-RFI 2016-00968), are acknowledged for assistance with the AFM measurements. We finally acknowledge financial support from the Swedish Foundation for Strategic Research, the Swedish Research Council, the Swedish Energy Agency, Stiftelsen Olle Engkvist Byggmästare, and Bertil & Britt Svenssons stiftelse för belysningsteknik.

■ REFERENCES

- (1) Hofmann, A. I.; Östergren, I.; Kim, Y.; Fauth, S.; Craighero, M.; Yoon, M.-H.; Lund, A.; Müller, C. All-Polymer Conducting Fibers and 3D Prints via Melt Processing and Templated Polymerization. *ACS Appl. Mater. Interfaces* **2020**, *12*, 8713–8721.
- (2) Yang, J. C.; Mun, J.; Kwon, S. Y.; Park, S.; Bao, Z. N.; Park, S. Electronic Skin: Recent Progress and Future Prospects for Skin-Attachable Devices for Health Monitoring, Robotics, and Prosthetics. *Adv. Mater.* **2019**, *31*, 1970337.
- (3) Paulsen, B. D.; Tybrandt, K.; Stavrinidou, E.; Rivnay, J. Organic mixed ionic-electronic conductors. *Nat. Mater.* **2020**, *19*, 13–26.
- (4) Zhang, Y.; Jie, J.; Sun, Y.; Jeon, S.-G.; Zhang, X.; Dai, G.; Lee, C. J.; Zhang, X. Precise Patterning of Organic Single Crystals via Capillary-Assisted Alternating-Electric Field. *Small* **2017**, *13*, 1604261.
- (5) Wang, H.; Deng, W.; Huang, L.; Zhang, X.; Jie, J. Precisely Patterned Growth of Ultra-Long Single-Crystalline Organic Micro-wire Arrays for Near-Infrared Photodetectors. *ACS Appl. Mater. Interfaces* **2016**, *8*, 7912–7918.
- (6) Gao, H.; Feng, J.; Zhang, B.; Xiao, C.; Wu, Y.; Kan, X.; Su, B.; Wang, Z.; Hu, W.; Sun, Y.; Jiang, L.; Heeger, A. J. Capillary-Bridge Mediated Assembly of Conjugated Polymer Arrays toward Organic Photodetectors. *Adv. Funct. Mater.* **2017**, *27*, 1701347.
- (7) Wang, B.; Ding, J.; Zhu, T.; Huang, W.; Cui, Z.; Chen, J.; Huang, L.; Chi, L. Fast patterning of oriented organic microstripes for field-effect ammonia gas sensors. *Nanoscale* **2016**, *8*, 3954–3961.
- (8) Zhu, X.; Liu, D.; Chen, Q.; Lin, L.; Jiang, S.; Zhou, H.; Zhao, J.; Wu, J. A paper-supported graphene–ionic liquid array for e-nose application. *Chem. Commun.* **2016**, *52*, 3042–3045.
- (9) Zhu, J.; Li, J.; Zhong, Q.; Wang, H.; Huang, L.; Fontein, F.; Hu, L.; Liu, R.; Fuchs, H.; Wang, W.; Wang, Y.; Chi, L. Lithography Compatible, Flexible Micro-Organic Light-Emitting Diodes by Template-Directed Growth. *Small Methods* **2019**, *3*, 1800508.
- (10) Cho, H.; Jeong, S.-H.; Min, S.-Y.; Han, T.-H.; Park, M.-H.; Kim, Y.-H.; Xu, W.; Lee, T.-W. Scalable Noninvasive Organic Fiber Lithography for Large-Area Optoelectronics. *Adv. Opt. Mater.* **2016**, *4*, 967–972.
- (11) Takeda, Y.; Yoshimura, Y.; Shiwa, R.; Hayasaka, K.; Sekine, T.; Okamoto, T.; Matsui, H.; Kumaki, D.; Katayama, Y.; Tokito, S. Organic Complementary Inverter Circuits Fabricated with Reverse Offset Printing. *Adv. Electron. Mater.* **2018**, *4*, 1700313.
- (12) Watson, C. P.; Brown, B. A.; Carter, J.; Morgan, J.; Taylor, D. M. Organic Ring Oscillators with Sub-200 ns Stage Delay Based on a Solution-Processed p-type Semiconductor Blend. *Adv. Electron. Mater.* **2016**, *2*, 1500322.
- (13) Oh, S.; Kim, J. H.; Park, S. K.; Ryoo, C. H.; Park, S. Y. Fabrication of Pixelated Organic Light-Emitting Transistor (OLET) with a Pure Red-Emitting Organic Semiconductor. *Adv. Opt. Mater.* **2019**, *7*, 1901274.

- (14) Park, H.-L.; Lee, B.; Kim, S.-U.; Suh, J.-H.; Kim, M.-H.; Lee, S.-D. Importance of surface modification of a microcontact stamp for pattern fidelity of soluble organic semiconductors. *J. Micro/Nanolithogr., MEMS, MOEMS* **2016**, *15*, 013501.
- (15) Kim, J.; Hassinen, T.; Lee, W. H.; Ko, S. Fully solution-processed organic thin-film transistors by consecutive roll-to-roll gravure printing. *Org. Electron.* **2017**, *42*, 361–366.
- (16) Briseno, A. L.; Aizenberg, J.; Han, Y.-J.; Penkala, R. A.; Moon, H.; Lovinger, A. J.; Kloc, C.; Bao, Z. Patterned Growth of Large Oriented Organic Semiconductor Single Crystals on Self-Assembled Monolayer Templates. *J. Am. Chem. Soc.* **2005**, *127*, 12164–12165.
- (17) Deng, W.; Zhang, X.; Dong, H.; Jie, J.; Xu, X.; Liu, J.; He, L.; Xu, L.; Hu, W.; Zhang, X. Channel-restricted meniscus self-assembly for uniformly aligned growth of single-crystal arrays of organic semiconductors. *Mater. Today* **2019**, *24*, 17–25.
- (18) Wang, B.; Zhu, T.; Huang, L.; Tam, T. L. D.; Cui, Z.; Ding, J.; Chi, L. Addressable growth of oriented organic semiconductor ultra-thin films on hydrophobic surface by direct dip-coating. *Org. Electron.* **2015**, *24*, 170–175.
- (19) Zhang, X.; Mao, J.; Deng, W.; Xu, X.; Huang, L.; Zhang, X.; Lee, S.-T.; Jie, J. Precise Patterning of Laterally Stacked Organic Microbelt Heterojunction Arrays by Surface-Energy-Controlled Stepwise Crystallization for Ambipolar Organic Field-Effect Transistors. *Adv. Mater.* **2018**, *30*, 1800187.
- (20) Hartl, H.; East, C.; Xu, Y.; Yambem, S. D.; Fairfull-Smith, K. E.; MacLeod, J. Direct-write crosslinking in vacuum-deposited small-molecule films using focussed ion and electron beams. *Nanotechnology* **2019**, *30*, 335301.
- (21) Tada, T.; Kanayama, T. Nanolithography Using Fullerene Films as an Electron Beam Resist. *Jpn. J. Appl. Phys., Part 2* **1996**, *35*, L63–L65.
- (22) Kim, J. S.; Kim, B. J.; Choi, Y. J.; Lee, M. H.; Kang, M. S.; Cho, J. H. An Organic Vertical Field-Effect Transistor with Underside-Doped Graphene Electrodes. *Adv. Mater.* **2016**, *28*, 4803–4810.
- (23) Lee, E. K.; Park, C. H.; Lee, J.; Lee, H. R.; Yang, C.; Oh, J. H. Chemically Robust Ambipolar Organic Transistor Array Directly Patterned by Photolithography. *Adv. Mater.* **2017**, *29*, 1605282.
- (24) Zhang, X.; Liu, F.; Li, H. Selective Photophysical Modification on Light-Emitting Polymer Films for Micro- and Nano-Patterning. *Materials* **2016**, *9*, 121.
- (25) Kahle, F.-J.; Saller, C.; Köhler, A.; Strohrriegel, P. Crosslinked Semiconductor Polymers for Photovoltaic Applications. *Adv. Energy Mater.* **2017**, *7*, 1700306.
- (26) Wang, G.-J. N.; Zheng, Y.; Zhang, S.; Kang, J.; Wu, H.-C.; Gasperini, A.; Zhang, H.; Gu, X.; Bao, Z. Tuning the Cross-Linker Crystallinity of a Stretchable Polymer Semiconductor. *Chem. Mater.* **2019**, *31*, 6465–6475.
- (27) Yum, J.-H.; Moon, S.-J.; Yao, L.; Caretti, M.; Nicolay, S.; Kim, D.-H.; Sivula, K. Robust Electron Transport Layers via In Situ Cross-Linking of Perylene Diimide and Fullerene for Perovskite Solar Cells. *ACS Appl. Energy Mater.* **2019**, *2*, 6616–6623.
- (28) Freudenberger, J.; Jänsch, D.; Hinkel, F.; Bunz, U. H. F. Immobilization Strategies for Organic Semiconducting Conjugated Polymers. *Chem. Rev.* **2018**, *118*, 5598–5689.
- (29) Burger, B.; Winter, J.; Kuzmany, H. Dimer and cluster formation in C60 photoreaction. *Z. Phys. B: Condens. Matter* **1996**, *101*, 227–233.
- (30) Distler, A.; Sauermann, T.; Egelhaaf, H.-J.; Rodman, S.; Waller, D.; Cheon, K.-S.; Lee, M.; Guldi, D. M. The Effect of PCBM Dimerization on the Performance of Bulk Heterojunction Solar Cells. *Adv. Energy Mater.* **2014**, *4*, 1300693.
- (31) Heumueller, T.; Mateker, W. R.; Distler, A.; Fritze, U. F.; Cheacharoen, R.; Nguyen, W. H.; Biele, M.; Salvador, M.; von Delius, M.; Egelhaaf, H.-J.; McGehee, M. D.; Brabec, C. J. Morphological and electrical control of fullerene dimerization determines organic photovoltaic stability. *Energy Environ. Sci.* **2016**, *9*, 247–256.
- (32) Dzwilewski, A.; Matyba, P.; Edman, L. Facile Fabrication of Efficient Organic CMOS Circuits. *J. Phys. Chem. B* **2010**, *114*, 135–140.
- (33) Dzwilewski, A.; Wågberg, T.; Edman, L. Photo-Induced and Resist-Free Imprint Patterning of Fullerene Materials for Use in Functional Electronics. *J. Am. Chem. Soc.* **2009**, *131*, 4006–4011.
- (34) Li, Z.; Wong, H. C.; Huang, Z.; Zhong, H.; Tan, C. H.; Tsoi, W. C.; Kim, J. S.; Durrant, J. R.; Cabral, J. T. Performance enhancement of fullerene-based solar cells by light processing. *Nat. Commun.* **2013**, *4*, 2227.
- (35) Dzwilewski, A.; Wågberg, T.; Edman, L. C-60 field-effect transistors: Effects of polymerization on electronic properties and device performance. *Phys. Rev. B: Condens. Matter Mater. Phys.* **2007**, *75*, 075203.
- (36) Rao, A. M.; Zhou, P.; Wang, K.-A.; Hager, G. T.; Holden, J. M.; Wang, Y.; Lee, W. T.; Bi, X.-X.; Eklund, P. C.; Cornett, D. S.; Duncan, M. A.; Amster, I. J. Photoinduced Polymerization of Solid C60 Films. *Science* **1993**, *259*, 955–957.
- (37) Zhou, P.; Dong, Z.-H.; Rao, A. M.; Eklund, P. C. Reaction mechanism for the photopolymerization of solid fullerene C60. *Chem. Phys. Lett.* **1993**, *211*, 337–340.
- (38) Barzegar, H. R.; Larsen, C.; Edman, L.; Wågberg, T. Solution-Based Phototransformation of C-60 Nanorods: Towards Improved Electronic Devices. *Part. Part. Syst. Charact.* **2013**, *30*, 715–720.
- (39) Wang, J.; Enevold, J.; Edman, L. Photochemical Transformation of Fullerenes. *Adv. Funct. Mater.* **2013**, *23*, 3220–3225.
- (40) Enevold, J.; Larsen, C.; Zakrisson, J.; Andersson, M.; Edman, L. Realizing Large-Area Arrays of Semiconducting Fullerene Nanostructures with Direct Laser Interference Patterning. *Nano Lett.* **2018**, *18*, 540–545.
- (41) Larsen, C.; Wang, J.; Edman, L. Complementary ring oscillator fabricated via direct laser-exposure and solution-processing of a single-layer organic film. *Thin Solid Films* **2012**, *520*, 3009–3012.
- (42) Lanz, T.; Sandström, A.; Tang, S.; Chabreck, P.; Sonderegger, U.; Edman, L. A light-emission textile device: conformal spray-sintering of a woven fabric electrode. *Flexible Printed Electron.* **2016**, *1*, 025004.
- (43) Lindh, E. M.; Lundberg, P.; Lanz, T.; Edman, L. Optical analysis of light-emitting electrochemical cells. *Sci. Rep.* **2019**, *9*, 10433.
- (44) Lindh, E. M.; Lundberg, P.; Lanz, T.; Mindemark, J.; Edman, L. The Weak Microcavity as an Enabler for Bright and Fault-tolerant Light-emitting Electrochemical Cells. *Sci. Rep.* **2018**, *8*, 6970.
- (45) Dmitruk, N. L.; Borkovskaya, O. Y.; Havrylenko, T. S.; Naumenko, D. O.; Petrik, P.; Meza-Laguna, V.; Basiuk, E. V. Effect of chemical modification of thin C60 fullerene films on the fundamental absorption edge. *Semicond. Phys., Quantum Electron. Optoelectron.* **2010**, *13*, 180–185.
- (46) Stangner, T.; Dahlberg, T.; Svenmarker, P.; Zakrisson, J.; Wiklund, K.; Oddershede, L. B.; Andersson, M. Cooke–Triplet tweezers: more compact, robust, and efficient optical tweezers. *Opt. Lett.* **2018**, *43*, 1990–1993.
- (47) Golan, L.; Reutsky, I.; Farah, N.; Shoham, S. Design and characteristics of holographic neural photo-stimulation systems. *J. Neural Eng.* **2009**, *6*, 066004.
- (48) Pekker, S.; Kamarás, K.; Kovács, É.; Pusztai, T.; Oszlányi, G. Isolation and structure of fullerene photodimer, C120. *AIP Conf. Proc.* **2001**, *591*, 37–40.
- (49) Bowman, R.; D'Ambrosio, V.; Rubino, E.; Jedrkiewicz, O.; Di Trapani, P.; Padgett, M. J. Optimisation of a low cost SLM for diffraction efficiency and ghost order suppression. *Eur. Phys. J.: Spec. Top.* **2011**, *199*, 149–158.
- (50) Hernandez, O.; Guillon, M.; Papagiakoumou, E.; Emiliani, V. Zero-order suppression for two-photon holographic excitation. *Opt. Lett.* **2014**, *39*, 5953–5956.
- (51) Pont, S.; Osella, S.; Smith, A.; Marsh, A. V.; Li, Z.; Beljonne, D.; Cabral, J. T.; Durrant, J. R. Evidence for Strong and Weak Phenyl-C-61-Butyric Acid Methyl Ester Photodimer Populations in Organic Solar Cells. *Chem. Mater.* **2019**, *31*, 6076–6083.
- (52) Xu, J.; Sandström, A.; Lindh, E. M.; Yang, W.; Tang, S.; Edman, L. Challenging Conventional Wisdom: Finding High-Performance

Electrodes for Light-Emitting Electrochemical Cells. *ACS Appl. Mater. Interfaces* **2018**, *10*, 33380–33389.

(53) Priebe, G.; Pietzak, B.; Könenkamp, R. Determination of transport parameters in fullerene films. *Appl. Phys. Lett.* **1997**, *71*, 2160–2162.

(54) Mort, J.; Machonkin, M.; Ziolo, R.; Chen, I. Electronic Carrier Transport And Photogeneration In Buckminsterfullerene Films. *Appl. Phys. Lett.* **1992**, *61*, 1829–1831.

(55) Sarkar, D.; Halas, N. J. Dember effect in C₆₀ thin films. *Solid State Commun.* **1994**, *90*, 261–265.

(56) Könenkamp, R.; Priebe, G.; Pietzak, B. Carrier mobilities and influence of oxygen in C₆₀ films. *Phys. Rev. B: Condens. Matter Mater. Phys.* **1999**, *60*, 11804–11808.

(57) Arbogast, J. W.; Foote, C. S.; Kao, M. Electron transfer to triplet fullerene C₆₀. *J. Am. Chem. Soc.* **1992**, *114*, 2277–2279.

(58) Wang, Y. Photoconductivity of fullerene-doped polymers. *Nature* **1992**, *356*, 585–587.

(59) Devišis, A.; De Jonghe-Risse, J.; Hany, R.; Nüesch, F.; Jenatsch, S.; Gulbinas, V.; Moser, J.-E. Dissociation of Charge Transfer States and Carrier Separation in Bilayer Organic Solar Cells: A Time-Resolved Electroabsorption Spectroscopy Study. *J. Am. Chem. Soc.* **2015**, *137*, 8192–8198.

(60) Matyba, P.; Maturova, K.; Kemerink, M.; Robinson, N. D.; Edman, L. The dynamic organic p–n junction. *Nat. Mater.* **2009**, *8*, 672–676.

(61) Wang, Z. B.; Helander, M. G.; Qiu, J.; Gao, D.; Chang, Y. L.; Lu, Z. H. C₆₀:LiF nanocomposite for high power efficiency fluorescent organic light-emitting diodes. *Nanotechnology* **2012**, *23*, 344010.

(62) Ren, S. L.; Wang, Y.; Rao, A. M.; McRae, E.; Holden, J. M.; Hager, T.; Wang, K.; Lee, W. T.; Ni, H. F.; Selegue, J.; Eklund, P. C. Ellipsometric determination of the optical constants of C₆₀ (Buckminsterfullerene) films. *Appl. Phys. Lett.* **1991**, *59*, 2678–2680.

(63) Richter, A.; Sturm, J. Dielectric and optical properties of C₆₀ material studied by ellipsometry and quantitative IR and UV/VIS spectroscopy. *Appl. Phys. A* **1995**, *61*, 163–170.

(64) Datta, D.; Kumar, S. Growth and ellipsometric studies on C₆₀ thin films for solar cell applications. *J. Appl. Phys.* **2009**, *106*, 074517.

(65) Kelly, M. K.; Etchegoin, P.; Fuchs, D.; Krättschmer, W.; Fostiropoulos, K. Optical transitions of C₆₀ films in the visible and ultraviolet from spectroscopic ellipsometry. *Phys. Rev. B: Condens. Matter Mater. Phys.* **1992**, *46*, 4963–4968.

(66) Shekhar, H.; Tzabari, L.; Solomeshch, O.; Tessler, N. Thickness dependent charge transfer states and dark carriers density in vacuum deposited small molecule organic photocell. *J. Appl. Phys.* **2016**, *120*, 155501.

(67) Lanz, T.; Lindh, E. M.; Edman, L. On the Asymmetric Evolution of the Optical Properties of a Conjugated Polymer during Electrochemical p- and n-type Doping. *J. Mater. Chem. C* **2017**, *5*, 4706–4715.

(68) Koh, T.-W.; Spechler, J. A.; Lee, K. M.; Arnold, C. B.; Rand, B. P. Enhanced Outcoupling in Organic Light-Emitting Diodes via a High-Index Contrast Scattering Layer. *ACS Photonics* **2015**, *2*, 1366–1372.

(69) Kwack, J. H.; Choi, J.; Park, C. H.; Hwang, H.; Park, Y. W.; Ju, B.-K. Simple method for fabricating scattering layer using random nanoscale rods for improving optical properties of organic light-emitting diodes. *Sci. Rep.* **2018**, *8*, 14311.

(70) Park, C. H.; Kim, J. G.; Jung, S.-G.; Lee, D. J.; Park, Y. W.; Ju, B.-K. Optical characteristics of refractive-index-matching diffusion layer in organic light-emitting diodes. *Sci. Rep.* **2019**, *9*, 8690.

(71) Loeser, F.; Romainczyk, T.; Rothe, C.; Pavicic, D.; Haldi, A.; Hofmann, M.; Murano, S.; Canzler, T.; Birnstock, J. Improvement of device efficiency in PIN-OLEDs by controlling the charge carrier balance and intrinsic outcoupling methods. *J. Photonics Energy* **2012**, *2*, 021207.

(72) Park, Y. C.; Choi, B. Enhanced Light Extraction from Bottom Emission OLEDs by High Refractive Index Nanoparticle Scattering Layer. *Nanomaterials* **2019**, *9*, 1241.

(73) Shin, J.-W.; Cho, H.; Lee, J.; Moon, J.; Han, J.-H.; Kim, K.; Cho, S.; Lee, J.-I.; Kwon, B.-H.; Cho, D.-H.; Lee, K. M.; Suemitsu, M.; Cho, N. S. Overcoming the efficiency limit of organic light-emitting diodes using ultra-thin and transparent graphene electrodes. *Opt. Express* **2018**, *26*, 617–626.